Available online at www.sciencedirect.com
SCIENCE DIRECT®
Journal of Sound and Vibration 283 (2005) 173–199
JOURNAL OF SOUND AND VIBRATION
www.elsevier.com/locate/jsvi

Freefield vibrations due to dynamic loading on a tunnel embedded in a stratified medium

D. Clouteau[a], M. Arnst[a,b], T.M. Al-Hussaini[a,c], G. Degrande[b,*]

[a]*MSSMat, UMR8579, Ecole Centrale Paris, Grande Voie des Vignes, F-92295 Chatenay-Malabry Cedex, France*
[b]*Department of Civil Engineering, K.U. Leuven, Kasteelpark Arenberg 40, B-3001 Leuven, Belgium*
[c]*Department of Civil Engineering, Bangladesh University of Engineering and Technology, Dhaka-1000, Bangladesh*

Received 1 November 2003; accepted 5 April 2004
Available online 14 October 2004

Abstract

An efficient and modular numerical prediction model is developed to predict vibration and re-radiated noise in adjacent buildings from excitation due to metro trains in tunnels for both newly built and existing situations. The three-dimensional dynamic tunnel–soil interaction problem is solved with a subdomain formulation, using a finite element formulation for the tunnel and a boundary element method for the soil. The periodicity of the tunnel and the soil in the longitudinal direction is exploited using the Floquet transform, limiting the discretization effort to a single bounded reference cell. It is demonstrated in the paper how the boundary element method can efficiently be extended to deal with periodic media, reusing the available three-dimensional Green's tensors for layered media. The efficiency of the method is demonstrated with a numerical example, where the case of harmonic and transient point loading on the invert of a shallow cut-and-cover masonry tunnel in Paris is considered. The work described here was carried out under the auspices of the CONVURT project sponsored by the European Community.

1. Introduction

Ground-borne vibrations induced by underground railways are transmitted to adjacent structures and are a major environmental concern in urban areas. Due to the highly complex

*Corresponding author. Tel.: +32-16-32-16-67; fax: +32-16-32-1988.
E-mail addresses: clouteau@mss.ecp.fr (D. Clouteau), geert.degrande@bwk.kuleuven.ac.be (G. Degrande).

0022-460X/$ - see front matter © 2004 Elsevier Ltd. All rights reserved.
doi:10.1016/j.jsv.2004.04.010

dynamic behaviour of such systems in the relevant frequency range between 0 and 100 Hz, mainly empirical methods have been considered in the past to characterize wave fields propagating away from tunnels. The aim of this paper is to show that advanced numerical models are able to give valuable insight and quantification of such phenomena in real situations. In particular, the case of a cut-and-cover shallow masonry tunnel embedded in a layered half-space is analyzed in detail.

As far as deterministic modelling is concerned, theoretical models with varying degree of sophistication have been proposed for trains running on the surface [1–3]. A model proposed by Krylov [4] for wave propagation in a homogeneous half-space due to moving axle loads has been extended [5–7] to include layered media and has been validated by means of experimental results. Recent track models [8,9] account for all relevant excitation mechanisms and for dynamic soil–structure interaction (SSI) at the track due to through-soil coupling of the sleepers on a ballasted track.

A review of models for trains running in tunnels has been presented by Kraft [10] and Hemsworth [11]. Two-dimensional finite element (FE) models with (local) absorbing boundary conditions [12] or analytical models [13] have been used, but these require major simplifications to translate the three-dimensional moving load into an equivalent line load and do not allow to incorporate three-dimensional structures. Moreover, two-dimensional models underestimate radiation damping in the soil and neglect wave propagation along the tunnel. These waves have been accounted for by Hunt [14], modelling the tunnel as an infinite cylinder in an infinite homogeneous full space. Alternatively, Stamos and Beskos [15,16] have used the boundary element (BE) method to compute the seismic response of tunnels.

Clouteau et al. [17,18] have proposed a general approach to track–vehicle interaction for translation invariant and periodic tracks. The fundamental ingredient of the models for track–vehicle interaction and radiation away from the tunnel is the transfer or Green's function of the track–tunnel–soil system.

As proposed by Clouteau et al. [19] in the case of earthquake engineering, the problem of tunnel–soil interaction is considered as a particular periodic case of a more general three-dimensional soil–structure interaction problem [20]. In this model, effects of nearby structures are neglected even though a periodic building model could have been included. The main objective here is the modelling of an equivalent three-dimensional incident field on a three-dimensional building. For the sake of simplicity, only point forces on the tunnel invert are accounted for and, once the corresponding time-varying three-dimensional solution is available, the response due to any moving load can be synthesized.

The objective of the present paper is to describe the development of an efficient and modular numerical prediction model for vibrations and re-radiated noise in adjacent buildings from excitation due to metro trains in tunnels for both newly built and existing situations, using recent developments in the area of dynamic soil–structure interaction analysis. These developments are one of the objectives of the EC Growth project CONVURT "The control of vibration from underground railway traffic".

Section 2 gives a brief description of the numerical model that is based on a BE formulation [18], modelling the soil as a three-dimensional horizontally layered medium, coupled with a FE formulation and modal reduction techniques for the tunnel. Due to the periodicity of the problem domain, the interaction problem can be transformed for any type of loading, including a point force, to a set of independent analyses on a bounded reference cell using the Floquet theorem.

Moreover, it is demonstrated that the proposed approach can reuse the existing three-dimensional BE technology for layered media as the periodic Green's kernels have the same singularities as the three-dimensional Green's kernels [21]. This is a major advantage compared to the so-called 2.5D approaches where a translation invariant model is assumed and for which the analysis of all singularities has to be repeated after the Fourier transform along the tunnel axis, except for surface tracks where the singular stress kernel vanishes [1]. Compared to earlier work of Clouteau et al. [21], a much more efficient way to compute the periodic Green's functions is proposed here, together with a novel way to build a modal basis on the tunnel that satisfies a priori the generalized periodicity conditions.

Within the frame of the CONVURT project, the numerical model is validated by means of in situ experiments at a site of the Cité Universitaire campus in Paris on the RER B line of RATP and a site in Regent's Park in London on the Bakerloo line of London Underground. Section 3 describes the first site and how it can be modelled using the proposed methodology. This section also reports on the convergence analysis that has been performed for this numerical model.

The harmonic and transient response due to point forces on the tunnel invert are subsequently discussed in Sections 4 and 5. Two simplified models are also used to explain the low-frequency resonance of the tunnel roof and the high-frequency filtering of the far field by the soil layering.

Section 6 finally summarizes the major contribution of this work and suggests some future refinements of the model.

2. Numerical modelling

2.1. Problem outline

The proposed model is based on the following hypotheses: (1) the tunnel is assumed to be periodic in the direction of its longitudinal axis $\mathbf{e}_2$ with a period L, (2) the tunnel is embedded in a horizontally layered soil, and (3) all displacements and strains remain sufficiently small so that linear models can be used. These hypotheses allow for the use of integral transforms along infinite directions of the model in order to restrict the analysis to bounded domains on which standard numerical techniques such as Galerkin formulations result in bounded discretization errors. These transforms are the Fourier transform with respect to time, the Floquet transform with respect to the periodic direction of the structure and the Hankel transform for the layered soil. Integral equations are used to express the coupling between the tunnel and the soil.

The physical domain is decomposed into two subdomains: the soil Ω_s and the tunnel Ω_t, as shown in Fig. 1. The interface between these subdomains is denoted by Σ_{ts}. The other boundaries are denoted by Γ_{sa}, Γ_{ta} and $\Gamma_{t\sigma}$, respectively. On Γ_{sa} and Γ_{ta}, free boundary conditions are assumed. On the boundary $\Gamma_{t\sigma}$, a surface force $\mathbf{f}_t$ is applied.

2.2. Governing equations

The permanent displacement fields on both subdomains Ω_α ($\alpha = s, t$) due to static loads are assumed to be known, so that $\mathbf{u}_\alpha$ denote the dynamic perturbations of the displacements in the soil and in the tunnel due to dynamic loads. These dynamic perturbations are assumed to be small

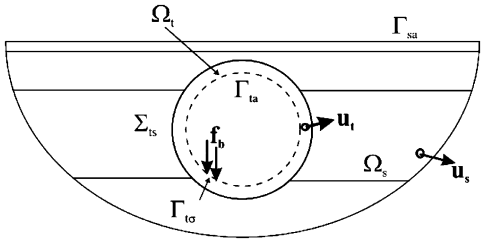

Fig. 1. Problem outline and notations.

enough to allow for a linear approximation of the constitutive equations in the vicinity of the static state. The dynamic perturbations $\boldsymbol{\sigma}_\alpha(\mathbf{u}_\alpha)$ of the stress tensors can be expressed as linear functions of the dynamic fluctuation of the strain tensors $\boldsymbol{\varepsilon}_\alpha(\mathbf{u}_\alpha)$, using Hooke's law:

$$\boldsymbol{\sigma}_\alpha(\mathbf{u}_\alpha) = \lambda_\alpha(\operatorname{div}\mathbf{u}_\alpha)\mathbf{I}_d + 2\mu_\alpha\boldsymbol{\varepsilon}_\alpha(\mathbf{u}_\alpha), \tag{1}$$

$$\boldsymbol{\varepsilon}_\alpha(\mathbf{u}_\alpha) = \tfrac{1}{2}[\operatorname{grad}\mathbf{u}_\alpha + (\operatorname{grad}\mathbf{u}_\alpha)^{\mathrm{T}}], \tag{2}$$

where λ_α and μ_α are the Lamé parameters with a possible small imaginary part to model hysteretic material damping and $\mathbf{I}_d$ is the 3×3 identity matrix. In the following, the traction vectors on an interface with an outer normal vector $\mathbf{n}$ are denoted by $\mathbf{t}_\alpha(\mathbf{u}_\alpha)$:

$$\mathbf{t}_\alpha(\mathbf{u}_\alpha) = \boldsymbol{\sigma}_\alpha(\mathbf{u}_\alpha)\mathbf{n}. \tag{3}$$

In the frequency domain, the complete system of Navier's equations and boundary conditions can be written as

The soil:

$$\mathbf{div}\,\boldsymbol{\sigma}_s(\mathbf{u}_s) = -\omega^2\rho_s\mathbf{u}_s \quad \text{in } \Omega_s, \tag{4}$$

$$\mathbf{t}_s(\mathbf{u}_s) = \mathbf{0} \quad \text{on } \Gamma_{sa}. \tag{5}$$

The tunnel:

$$\mathbf{div}\,\boldsymbol{\sigma}_t(\mathbf{u}_t) = -\omega^2\rho_t\mathbf{u}_t \quad \text{in } \Omega_t, \tag{6}$$

$$\mathbf{t}_t(\mathbf{u}_t) = \mathbf{0} \quad \text{on } \Gamma_{ta}, \tag{7}$$

$$\mathbf{t}_t(\mathbf{u}_t) = \mathbf{f}_t \quad \text{on } \Gamma_{t\sigma}. \tag{8}$$

Compatibility and equilibrium:

$$\mathbf{u}_s = \mathbf{u}_t \quad \text{on } \Sigma_{ts}, \tag{9}$$

$$\mathbf{t}_s(\mathbf{u}_s) + \mathbf{t}_t(\mathbf{u}_t) = \mathbf{0} \quad \text{on } \Sigma_{ts}, \tag{10}$$

together with radiation conditions for the displacement field in the soil.

2.3. Periodic approach of dynamic soil–tunnel interaction

The problem of dynamic soil–tunnel interaction is a three-dimensional problem with a periodicity with period L in the longitudinal direction $\mathbf{e}_2$ along the tunnel axis. The position vector

$\mathbf{x}$ of any point in the problem domain Ω is decomposed as

$$\mathbf{x} = \tilde{\mathbf{x}} + nL\mathbf{e}_2, \tag{11}$$

where $\tilde{\mathbf{x}}$ is the position vector in the reference cell $\tilde{\Omega}$ and n is the cell number. A Floquet transformation is used to transform the distance nL between the nth cell and the reference cell $\tilde{\Omega}$ to the wave number κ and to restrict the model to periodic fields of the second kind defined on a single reference cell [22]. Cells, periodic fields of the second kind and Floquet transforms have the following definitions and properties:

Definition (*Generic cell*). The generic cell $\tilde{\Omega}$ of a periodic domain Ω is defined as

$$\tilde{\Omega} = \left\{ \mathbf{x} \in \Omega | -\frac{L}{2} \leqslant \mathbf{x} \cdot \mathbf{e}_2 \leqslant +\frac{L}{2} \right\}. \tag{12}$$

Definition (*Periodicity of the second kind*). A complex valued function $\tilde{f}(\tilde{\mathbf{x}}, \kappa)$, defined on a periodic domain Ω, is periodic of the second kind with a period L in the direction $\mathbf{e}_2$ and wavenumber κ, if for all $\mathbf{x} \in \Omega$,

$$\tilde{f}(\tilde{\mathbf{x}} + L\mathbf{e}_2, \kappa) = \mathrm{e}^{-\mathrm{i}\kappa L}\tilde{f}(\tilde{\mathbf{x}}, \kappa). \tag{13}$$

It is strictly periodic or periodic of the first kind when $L = 0$:

$$\tilde{f}(\tilde{\mathbf{x}} + L\mathbf{e}_2, \kappa) = \tilde{f}(\tilde{\mathbf{x}}, \kappa). \tag{14}$$

This definition can be extended as follows to operators with periodic coefficients:

Definition (*Periodic operator of the first kind*). The operator $\mathscr{A}$ with domain $D(\mathscr{A})$ is periodic of the first kind with period L in the direction $\mathbf{e}_2$ if

$$\forall \mathbf{u} \in D(\mathscr{A})\ \forall \mathbf{x} \in \Omega: \mathscr{A}(\mathbf{x} + L\mathbf{e}_2)\mathbf{u} = \mathscr{A}(\mathbf{x})\mathbf{u}. \tag{15}$$

The periodicity of the first kind of $\mathscr{A}$ allows for a computation on the generic cell, with a restriction of its domain to periodic fields of the second kind with support on that cell. Any field on a periodic domain can indeed be transformed to periodic fields using the so-called Floquet transform:

Definition (*The Floquet transform*). Let $f(\mathbf{x})$ be a function defined on a periodic domain Ω with values in $\mathbb{C}$ and let L be the geometrical period along the direction $\mathbf{e}_2$. The Floquet transform $\tilde{f}(\tilde{\mathbf{x}}, \kappa)$ of the function $f(\mathbf{x})$ is the complex valued function of the spatial coordinate $\tilde{\mathbf{x}}$ on the generic cell and of the wavenumber κ:

$$\tilde{\Omega} \times]-\pi/L, +\pi/L[\to \mathbb{C} : \tilde{f}(\tilde{\mathbf{x}}, \kappa) = \sum_{n=-\infty}^{+\infty} f(\tilde{\mathbf{x}} + nL\mathbf{e}_2)\mathrm{e}^{\mathrm{i}n\kappa L}. \tag{16}$$

The inverse Floquet transform is defined as

$$f(\mathbf{x}) = \frac{L}{2\pi}\int_{-\pi/L}^{+\pi/L} \tilde{f}(\tilde{\mathbf{x}},\kappa)\mathrm{e}^{-\mathrm{i}n\kappa L}\,\mathrm{d}\kappa. \tag{17}$$

When (16) is extended to the entire domain $\Omega \times \mathbb{R}$, the transformed function $\tilde{f}(\tilde{\mathbf{x}},\kappa)$ is periodic of the second kind with respect to $\tilde{\mathbf{x}}$ and periodic of the first kind with respect to κ with a period of $2\pi/L$.

By construction, the system of equations (4)–(10) defines a periodic operator $\mathscr{A}$ of the first kind, which can be restricted to a reference cell provided that a Floquet transform is applied to the original fields. Once known, the displacement and traction fields obtained in the spatial-wavenumber domain can be inverse Floquet transformed to their values in the spatial-frequency domain.

2.4. Dynamic soil–structure interaction in the frequency-wavenumber domain

As mentioned, the problem is restricted to a single generic cell $\tilde{\Omega}$. The domains Ω_t and Ω_s are restricted to the domains $\tilde{\Omega}_t$ and $\tilde{\Omega}_s$, respectively; the boundaries Γ_{sa}, Γ_{ta}, $\Gamma_{t\sigma}$ and the interface Σ_{ts} are restricted to $\tilde{\Gamma}_{sa}$, $\tilde{\Gamma}_{ta}$, $\tilde{\Gamma}_{t\sigma}$ and the interface $\tilde{\Sigma}_{ts}$. All displacement and traction fields $\mathbf{u}(\mathbf{x},\omega)$ and $\mathbf{t}(\mathbf{x},\omega)$ defined on the periodic domain Ω are transformed to the fields $\tilde{\mathbf{u}}(\tilde{\mathbf{x}},\kappa,\omega)$ and $\tilde{\mathbf{t}}(\tilde{\mathbf{x}},\kappa,\omega)$ defined on the generic cell $\tilde{\Omega}$.

The equilibrium of the tunnel is written in a weak sense. The tunnel displacements $\tilde{\mathbf{u}}_t(\tilde{\mathbf{x}},\kappa,\omega)$ must satisfy the equilibrium equation (10), transformed to the wavenumber domain. Multiplying this equation with the complex conjugate of any virtual field $\tilde{\mathbf{v}}_t(\tilde{\mathbf{x}},\kappa)$ and integrating over the domain $\tilde{\Omega}_t$ yields

$$\int_{\tilde{\Omega}_t} \tilde{\boldsymbol{\sigma}}(\tilde{\mathbf{u}}_t) : \overline{\tilde{\boldsymbol{\varepsilon}}(\tilde{\mathbf{v}}_t)}\,\mathrm{d}V - \omega^2\int_{\tilde{\Omega}_t} \rho_t\tilde{\mathbf{u}}_t\cdot\overline{\tilde{\mathbf{v}}_t}\,\mathrm{d}V = \int_{\partial\tilde{\Omega}_{bt}} \tilde{\mathbf{t}}_t(\tilde{\mathbf{u}}_t)\cdot\overline{\tilde{\mathbf{v}}_t}\,\mathrm{d}S + \int_{\tilde{\Gamma}_{t\sigma}} \tilde{\mathbf{f}}_t\cdot\overline{\tilde{\mathbf{v}}_t}\,\mathrm{d}S, \tag{18}$$

where the boundary $\partial\tilde{\Omega}_t$ of $\tilde{\Omega}_t$ can be decomposed into the tunnel–soil interface $\tilde{\Sigma}_{ts}$ and $\Sigma_0 \cup \Sigma_L$, the two boundaries of $\tilde{\Omega}_t$ at the two edges $\tilde{y} = \pm L/2$ of the generic cell. As the actual and the virtual displacement fields are periodic of the second kind, the integral on the right-hand side of Eq. (18) on the sum of the two boundaries Σ_0 and Σ_L vanishes [21]. Accounting for stress equilibrium (10) along the tunnel–soil interface $\tilde{\Sigma}_{ts}$, the equilibrium equation (18) becomes

$$\int_{\tilde{\Omega}_t} \tilde{\boldsymbol{\sigma}}(\tilde{\mathbf{u}}_t) : \overline{\tilde{\boldsymbol{\varepsilon}}(\tilde{\mathbf{v}}_t)}\,\mathrm{d}V - \omega^2\int_{\tilde{\Omega}_t} \rho_t\tilde{\mathbf{u}}_t\cdot\overline{\tilde{\mathbf{v}}_t}\,\mathrm{d}V + \int_{\tilde{\Sigma}_{ts}} \tilde{\mathbf{t}}_s(\tilde{\mathbf{u}}_s)\cdot\overline{\tilde{\mathbf{v}}_t}\,\mathrm{d}S = \int_{\tilde{\Gamma}_{t\sigma}} \tilde{\mathbf{f}}_t\cdot\overline{\tilde{\mathbf{v}}_t}\,\mathrm{d}S. \tag{19}$$

Since the generic cell $\tilde{\Omega}_t$ of the tunnel is bounded, the displacement field $\tilde{\mathbf{u}}_t(\tilde{\mathbf{x}},\kappa,\omega)$ can be expanded with bounded error on a finite basis of displacement fields $\tilde{\boldsymbol{\psi}}_m(\tilde{\mathbf{x}},\kappa)$ $(m = 1,\ldots,N)$, provided that these fields are periodic of the second kind:

$$\tilde{\mathbf{u}}_t(\tilde{\mathbf{x}},\kappa,\omega) = \sum_{m=1}^{N} c_m(\kappa,\omega)\tilde{\boldsymbol{\psi}}_m(\tilde{\mathbf{x}},\kappa) \quad \text{in } \tilde{\Omega}_t. \tag{20}$$

Accounting for the displacement compatibility equation (9) and the linearity of the problem, the soil displacements $\tilde{\mathbf{u}}_s(\tilde{\mathbf{x}},\kappa,\omega)$ can be written as

$$\tilde{\mathbf{u}}_s(\tilde{\mathbf{x}},\kappa,\omega)=\sum_{m=1}^{N} c_m(\kappa,\omega)\tilde{\mathbf{u}}_{dm}(\tilde{\mathbf{x}},\kappa,\omega) \quad \text{in } \tilde{\Omega}_s, \tag{21}$$

where the elastodynamic field $\tilde{\mathbf{u}}_{dm}(\tilde{\mathbf{x}},\kappa,\omega)$ satisfies the radiation condition, the free boundary condition and the following condition on the boundary $\tilde{\Sigma}_{ts}$:

$$\tilde{\mathbf{u}}_{dm}(\tilde{\mathbf{x}},\kappa,\omega)=\tilde{\boldsymbol{\psi}}_m(\tilde{\mathbf{x}},\kappa) \quad \text{on } \tilde{\Sigma}_{ts}. \tag{22}$$

Each elastodynamic field $\tilde{\mathbf{u}}_{dm}(\tilde{\mathbf{x}},\kappa,\omega)$ creates a traction field $\tilde{\mathbf{t}}_{dm}(\tilde{\mathbf{x}},\kappa,\omega)=\tilde{\mathbf{t}}_s(\tilde{\mathbf{u}}_{dm})(\tilde{\mathbf{x}},\kappa,\omega)$ on the tunnel–soil interface, so that the tractions in the soil $\tilde{\mathbf{t}}_s(\tilde{\mathbf{u}}_s)(\tilde{\mathbf{x}},\kappa,\omega)$ are decomposed as follows:

$$\tilde{\mathbf{t}}_s(\tilde{\mathbf{u}}_s)(\tilde{\mathbf{x}},\kappa,\omega)=\sum_{m=1}^{N} c_m(\kappa,\omega)\tilde{\mathbf{t}}_{dm}(\tilde{\mathbf{x}},\kappa,\omega) \quad \text{on } \tilde{\Sigma}_{ts}. \tag{23}$$

Expansions (20) and (23) are introduced in the variational formulation (19), with $\tilde{\mathbf{v}}_t(\tilde{\mathbf{x}},\kappa)=\tilde{\boldsymbol{\psi}}_n(\tilde{\mathbf{x}},\kappa)$. This results into the following system of equations for the vector of generalized degrees of freedom $\mathbf{c}(\kappa,\omega)$, describing the dynamic tunnel–soil interaction problem in the frequency-wavenumber domain:

$$[\mathbf{K}_t(\kappa)-\omega^2\mathbf{M}_t(\kappa)+\mathbf{K}_s(\kappa,\omega)]\mathbf{c}(\kappa,\omega)=\mathbf{f}_t(\kappa,\omega) \tag{24}$$

with $\mathbf{K}_t(\kappa)$ and $\mathbf{M}_t(\kappa)$ the stiffness and mass matrices of the tunnel, $\mathbf{K}_s(\kappa,\omega)$ the dynamic stiffness matrix of the soil and $\mathbf{f}_t(\kappa,\omega)$ the generalized force vector applied on the tunnel invert, defined as

$$[\mathbf{K}_t]_{nm}=\int_{\tilde{\Omega}_t}\tilde{\boldsymbol{\sigma}}(\tilde{\boldsymbol{\psi}}_m):\overline{\tilde{\boldsymbol{\varepsilon}}(\tilde{\boldsymbol{\psi}}_n)}\,\mathrm{d}V, \quad [\mathbf{M}_t]_{nm}=\int_{\tilde{\Omega}_t}\rho_t\tilde{\boldsymbol{\psi}}_m\cdot\overline{\tilde{\boldsymbol{\psi}}_n}\,\mathrm{d}V, \tag{25}$$

$$[\mathbf{K}_s]_{nm}=\int_{\tilde{\Sigma}_{ts}}\tilde{\mathbf{t}}_{dm}\cdot\overline{\tilde{\boldsymbol{\psi}}_n}\,\mathrm{d}S, \quad [\mathbf{f}_t]_n=\int_{\tilde{\Gamma}_{t\sigma}}\tilde{\mathbf{f}}_t\cdot\overline{\tilde{\boldsymbol{\psi}}_n}\,\mathrm{d}S. \tag{26}$$

Let us consider a finite element model of the tunnel's reference cell with M_{dof} degrees of freedom and define $\tilde{\boldsymbol{\Psi}}(\kappa)$ as the $M_{\mathrm{dof}}\times N$ matrix containing the N modes $\tilde{\boldsymbol{\psi}}_m(\kappa)$. If $\mathbf{K}^{\mathrm{FEM}}$ and $\mathbf{M}^{\mathrm{FEM}}$ are the standard $M_{\mathrm{dof}}\times M_{\mathrm{dof}}$ finite element stiffness and mass matrices, then the matrices $\mathbf{M}_t(\kappa)$ and $\mathbf{K}_t(\kappa)$ are given by

$$\mathbf{K}_t(\kappa)=\overline{\tilde{\boldsymbol{\Psi}}(\kappa)}^{\mathrm{T}}\mathbf{K}^{\mathrm{FEM}}\tilde{\boldsymbol{\Psi}}(\kappa), \quad \mathbf{M}_t(\kappa)=\overline{\tilde{\boldsymbol{\Psi}}(\kappa)}^{\mathrm{T}}\mathbf{M}^{\mathrm{FEM}}\tilde{\boldsymbol{\Psi}}(\kappa). \tag{27}$$

2.5. Kinematic basis for the tunnel

To take into account the periodicity, the kinematic basis for the tunnel has to be determined in such a way that the fields $\tilde{\boldsymbol{\psi}}_m(\tilde{\mathbf{x}},\kappa)$ are satisfying the following relationship between both ends of the cell:

$$\tilde{\boldsymbol{\psi}}_m(\tilde{\mathbf{x}}+L\mathbf{e}_2,\kappa)=\mathrm{e}^{-\mathrm{i}\kappa L}\tilde{\boldsymbol{\psi}}_m(\tilde{\mathbf{x}},\kappa) \quad \forall\tilde{\mathbf{x}}\in\tilde{\Omega}_t\,|\,\tilde{\mathbf{x}}\cdot\mathbf{e}_2=-\frac{L}{2}. \tag{28}$$

Assuming that modes $\tilde{\boldsymbol{\psi}}_m^o$ can be built that satisfy for $\kappa = 0$:

$$\tilde{\boldsymbol{\psi}}_m^0(\tilde{\mathbf{x}} + L\mathbf{e}_2) = \tilde{\boldsymbol{\psi}}_m^0(\tilde{\mathbf{x}}) \quad \forall \tilde{\mathbf{x}} \in \tilde{\Omega}_t \mid \tilde{\mathbf{x}} \cdot \mathbf{e}_2 = -\frac{L}{2} \tag{29}$$

the fields $\tilde{\boldsymbol{\psi}}_m(\tilde{\mathbf{x}}, \kappa)$ that satisfy the periodicity condition of the second kind for non-vanishing wavenumber κ can be built as follows:

$$\tilde{\boldsymbol{\psi}}_m(\tilde{\mathbf{x}}, \kappa) = \mathrm{e}^{-\mathrm{i}\kappa \mathbf{e}_2 \cdot \tilde{\mathbf{x}}} \tilde{\boldsymbol{\psi}}_m^0(\tilde{\mathbf{x}}). \tag{30}$$

In a finite element context, the phase term $\mathrm{e}^{-\mathrm{i}\kappa \mathbf{e}_2 \cdot \tilde{\mathbf{x}}}$ can be interpolated at each node, generating an M_{dof}-dimensional diagonal matrix $\boldsymbol{\Lambda}(\kappa)$. The wavenumber-dependent modes $\tilde{\boldsymbol{\Psi}}(\tilde{\mathbf{x}}, \kappa)$ are obtained by multiplying the strictly periodic modes $\tilde{\boldsymbol{\Psi}}^0(\tilde{\mathbf{x}})$ by $\boldsymbol{\Lambda}(\kappa)$. Moreover, the development of $\boldsymbol{\Lambda}(\kappa)$ for small wavenumbers shows that, at a given frequency ω, the dynamic stiffness matrix of the tunnel is quadratic with respect to the wavenumber κ as it is quadratic with respect to the frequency for a given wavenumber. These results show that the stiffness of the tunnel increases with increasing wavenumber. It can be observed that, unless hysteretic or viscous damping is added in the model, the dynamic stiffness matrix of the tunnel remains strictly real valued. These results will be totally different for the dynamic stiffness matrix of the soil due to the unboundedness of the soil domain. Another numerical technique than the standard finite element method is required to model the soil domain.

2.6. The periodic boundary element method

The dynamic stiffness matrix of a foundation embedded in a homogeneous or layered half-space is classically computed using a boundary element method, as this numerical technique directly gives the traction field $\mathbf{t}_{dm}$ on the foundation as a function of the imposed displacement field $\boldsymbol{\psi}_m$, allowing for a computation of the dynamic stiffness matrix $\mathbf{K}_s$ using Eq. (26). Following this line of thought for the periodic case would consist in demonstrating that the Floquet transform can commute with the standard boundary integral equation. This work has been performed by Elhabre [22] who has built a new fundamental solution that satisfies the periodicity condition and is referred to as the Green–Floquet function.

Definition (*The Green–Floquet function*). Let $\mathbf{u}^G(\mathbf{x}, \mathbf{y}, \mathbf{a}; \omega)$ be the Green's function of a periodic domain, e.g. the displacement at a point $\mathbf{x}$ generated by a point force $\mathbf{a}$ at a point $\mathbf{y}$. The Green–Floquet fundamental solution $\tilde{\mathbf{u}}^{GF}(\tilde{\mathbf{x}}, \tilde{\mathbf{y}}, \mathbf{a}; \kappa, \omega)$ is defined as the infinite sum of Green's functions at the point $\mathbf{x}$ for sources that are periodically located in space at $\tilde{\mathbf{y}} + nL\mathbf{e}_2$ and with a phase shift $\mathrm{e}^{\mathrm{i}\kappa L}$ between two adjacent locations:

$$\tilde{\mathbf{u}}^{GF}(\tilde{\mathbf{x}}, \tilde{\mathbf{y}}, \mathbf{a}; \kappa, \omega) = \sum_{n=-\infty}^{+\infty} \mathrm{e}^{\mathrm{i}n\kappa L} \mathbf{u}^G(\tilde{\mathbf{x}}, \tilde{\mathbf{y}} + nL\mathbf{e}_2, \mathbf{a}; \omega). \tag{31}$$

The Green–Floquet fundamental solution is periodic of the second kind with respect to $\tilde{\mathbf{x}}$ and $\tilde{\mathbf{y}}$ with a period L in the direction $\mathbf{e}_2$ and wavenumbers $-\kappa$ and κ, respectively:

$$\tilde{\mathbf{u}}^{GF}(\tilde{\mathbf{x}}, \tilde{\mathbf{y}} + L\mathbf{e}_2, \mathbf{a}; \kappa, \omega) = \mathrm{e}^{-\mathrm{i}\kappa L} \tilde{\mathbf{u}}^{GF}(\tilde{\mathbf{x}}, \tilde{\mathbf{y}}, \mathbf{a}; \kappa, \omega), \tag{32}$$

$$\tilde{\mathbf{u}}^{GF}(\tilde{\mathbf{x}} + L\mathbf{e}_2, \tilde{\mathbf{y}}, \mathbf{a}; \kappa, \omega) = \mathrm{e}^{\mathrm{i}\kappa L} \tilde{\mathbf{u}}^{GF}(\tilde{\mathbf{x}}, \tilde{\mathbf{y}}, \mathbf{a}; \kappa, \omega). \tag{33}$$

Using this Green–Floquet fundamental solution, the following direct boundary integral equation on the reference cell is obtained for a homogeneous or a layered medium [22]:

$$\int_{\tilde{\Sigma}_{ts}} \tilde{\mathbf{t}}(\tilde{\mathbf{u}})(\tilde{\mathbf{x}}) \cdot \tilde{\mathbf{u}}^{GF}(\tilde{\mathbf{x}}, \tilde{\boldsymbol{\xi}}, \mathbf{a})\, \mathrm{d}S - \oint_{\tilde{\Sigma}_{ts}} \tilde{\mathbf{t}}(\tilde{\mathbf{u}}^{GF}(\tilde{\mathbf{x}}, \tilde{\boldsymbol{\xi}}, \mathbf{a})) \cdot \tilde{\mathbf{u}}(\tilde{\mathbf{x}})\, \mathrm{d}S = \mathbf{C}(\tilde{\boldsymbol{\xi}}) : (\tilde{\mathbf{u}}(\tilde{\boldsymbol{\xi}}) \otimes \mathbf{a}), \tag{34}$$

where $\mathbf{C}(\tilde{\boldsymbol{\xi}})$ is the integral free term that is equal to $1/2\mathbf{I}_d$ for a locally homogeneous and smooth interface.

It is worth noting that only the bounded tunnel–soil interface $\tilde{\Sigma}_{ts}$ appears in Eq. (34), whereas the unbounded part of the boundary of $\tilde{\Omega}_s$, consisting of the two edges Σ_0 and Σ_L of the reference cell, has disappeared. The major advantage of using the Green–Floquet fundamental solution is indeed that the periodic boundary conditions on these boundaries are implicitly accounted for in Eq. (34). This is similar as for the case of the free surface condition using the fundamental solution of the half-space. The boundaries Σ_0 and Σ_L therefore do not need to be discretized.

The second advantage, compared to a translational invariant solution proposed by Aubry et al. [1], is that the Green–Floquet solution $\tilde{\mathbf{u}}^{GF}(\tilde{\mathbf{x}}, \tilde{\mathbf{y}}, \mathbf{a}; \kappa, \omega)$ has the same singularities as the original Green's function $\mathbf{u}^{G}(\mathbf{x}, \mathbf{y}, \mathbf{a}; \omega)$, so that the same numerical integration method can be used. Consequently, the numerical implementation is straightforward: the bounded interface $\tilde{\Sigma}_{ts}$ is meshed and a collocation or a variational method is applied, resulting into the following system of equations for the traction vector $\tilde{\mathbf{t}}(\kappa, \omega)$ with dimension $3N_e$:

$$[\tilde{\mathbf{U}}^{GF}(\kappa, \omega)]\tilde{\mathbf{t}}(\kappa, \omega) = \mathbf{b}(\kappa, \omega) \tag{35}$$

with

$$[\tilde{\mathbf{U}}^{GF}(\kappa, \omega)]_{EiFk} = \int_F \int_E \mathbf{e}_i \cdot \tilde{\mathbf{u}}^{GF}(\tilde{\mathbf{x}}_E, \tilde{\boldsymbol{\xi}}_F, \mathbf{e}_k; \kappa, \omega)\, \mathrm{d}S(\tilde{\mathbf{x}}_E)\, \mathrm{d}S(\tilde{\boldsymbol{\xi}}_F) \tag{36}$$

and

$$[\mathbf{b}]_{Fk} = \int_F \oint_E \mathbf{u} \cdot \tilde{\mathbf{t}}_n(\tilde{\mathbf{u}}^{GF})(\tilde{\mathbf{x}}_E, \tilde{\boldsymbol{\xi}}_F, \mathbf{e}_k; \kappa, \omega)\, \mathrm{d}S(\tilde{\mathbf{x}}_E)\, \mathrm{d}S(\tilde{\boldsymbol{\xi}}_F) + \int_F \mathbf{e}_k^{\mathrm{T}} \mathbf{C} \tilde{\mathbf{u}}(\tilde{\boldsymbol{\xi}}_F)\, \mathrm{d}S(\tilde{\boldsymbol{\xi}}_F). \tag{37}$$

As far as the numerical implementation is concerned, the infinite series of Green's functions in Eq. (31) is approximated by a finite sum ($n = -N_c$ to N_c). The integrals in Eqs. (36) and (37) are approximated numerically using Gauss quadrature. Eq. (36) yields

$$\tilde{\mathbf{U}}^{GF}(\kappa, \omega) \approx \sum_{n=-N_c}^{+N_c} \mathrm{e}^{\mathrm{i}n\kappa L} \tilde{\mathbf{U}}_n^{G}(\omega), \tag{38}$$

where

$$[\mathbf{U}_n^{G}(\omega)]_{EiFk} \approx \sum_{q=1}^{N_q} \sum_{q'=1}^{N'_q} w_{Eq} w_{Fq'} \mathbf{u}^{G}(\tilde{\mathbf{x}}_q, \tilde{\boldsymbol{\xi}}_{q'} + nL\mathbf{e}_2, \mathbf{e}_k; \omega) \cdot \mathbf{e}_i. \tag{39}$$

The matrix $\tilde{\mathbf{U}}_0^G(\omega)$ is the standard 3D boundary element matrix, while the matrices $\tilde{\mathbf{U}}_n^G(\omega)$ with $n \neq 0$ are computed translating the sources $\tilde{\boldsymbol{\xi}}_F$ over a distance $nL\mathbf{e}_2$. A moderate computational effort is needed, as the computation of the matrices $\tilde{\mathbf{U}}^{GF}(\kappa, \omega)$ for all wavenumbers κ requires only a single calculation of the matrices $\tilde{\mathbf{U}}_n^G(\omega)$. Moreover, when n is large enough, the distance between the sources $\tilde{\boldsymbol{\xi}}_{q'} + nL\mathbf{e}_2$ and the receivers $\tilde{\mathbf{x}}_q$ is large as well and the Green function varies smoothly over elements E and F, requiring very few Gauss points in the computation of the sum in Eq. (39).

3. Numerical example

3.1. Problem outline

In this section, results of numerical computations of ground vibration at the site of Cité Universitaire site in Paris will be presented. This site is located on the line RER B between the metro stations Cité Universitaire and Gentilly and is one of sites that has been selected in the CONVURT project to perform elaborate in situ measurements for the validation of the numerical model.

The metro tunnel on the line RER B at Cité Universitaire is a masonry cut-and-cover tunnel with two tracks at a shallow depth of about 9.3 m below the free surface. Fig. 2 shows one symmetrical half of the tunnel's cross-section, as well as the modelled soil stratigraphy. The top of the tunnel is 2.3 m below the ground surface. The thickness of the tunnel is equal to 0.6 m at the top, while the slab thickness is equal to 0.4 m and the wall thickness is equal to 1.5 m.

In the model, the masonry is assumed to have a Young's modulus of 14 GPa, a Poisson ratio of 0.15, a mass density of 2400 kg/m^3 and a hysteresis damping ratio of 2%.

The tunnel is considered to be infinitely long with an invariant cross-section. As discussed in Section 2, the problem can be reduced to a single reference cell, as shown in Fig. 3. The period is equal to $L = 0.3$ m in the y-direction. The tunnel is modelled using 8-node isoparametric brick elements as shown in Fig. 3. For the sake of simplicity, the ballast, the sleepers and the track are not (yet) included in the model, as their influence on the dynamic behavior of the tunnel–soil system is only important for frequencies larger than 80 Hz.

The soil stratigraphy is in accordance with preliminary results of SASW tests that have been performed to determine the thickness and the dynamic characteristics of the shallow soil layers [23]. The tests have been performed on two measurement lines perpendicular and parallel to the tunnel. The results demonstrate the presence of a shallow layer with a thickness of approximately 1.4 m and a shear wave velocity $C_s = 115$ m/s, a stiffer layer with a thickness of 2.8 m and a shear wave velocity $C_s = 220$ m/s on top of a half-space with a shear wave velocity $C_s = 315$ m/s. The stratigraphy is summarized in Table 1. A hysteresis damping ratio of 5% is assumed for all three materials.

In the following subsections, results are presented for the vibrations of the tunnel and the soil in the free field due to a non-moving harmonic or transient excitation on the tunnel invert at a position with coordinates $(-2.5, 0.0, -8.25)$ in the frame of reference defined in Fig. 3. This force is Floquet transformed to the wavenumber domain, resulting into two equivalent forces applied on two nodes of the finite element model of the generic cell (Fig. 3). The spectral content of these

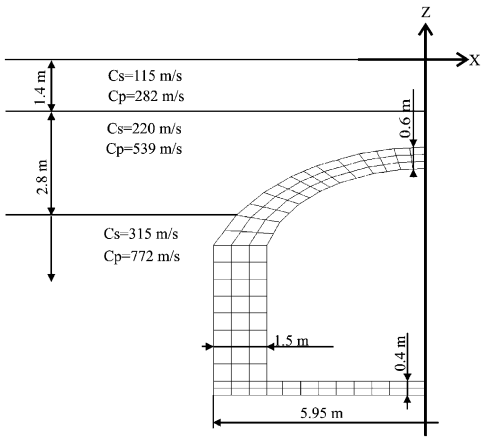

Fig. 2. Cross-section of the metro tunnel on the line RER B of RATP at Cité Universitaire.

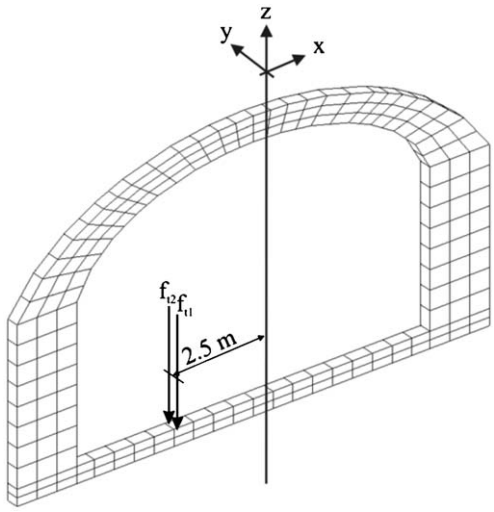

Fig. 3. Finite element model of the reference cell and position of the forces on the tunnel invert.

forces in the wavenumber domain is uniform and equal to 0.5. After the computation of the response of the generic cell in the wavenumber-frequency domain, the results are transformed to the spatial domain and animated on the mesh shown in Fig. 4.

3.2. Convergence analysis

A kinematic basis for the tunnel is determined, consisting of modes $\tilde{\boldsymbol{\psi}}_m(\tilde{\mathbf{x}}, \kappa)$ derived from the eigenmodes $\boldsymbol{\psi}_m^0(\tilde{\mathbf{x}})$ of the generic tunnel cell with free boundary conditions on Σ_{ts} and satisfying the supplementary periodicity constraints given by Eq. (30). Due to these constraints and the symmetry of the cell, displacements in the y-direction are decoupled from displacements in the

Table 1
The stratigraphy of the soil

Layer	Thickness (m)	C_s (m/s)	C_p (m/s)	ρ (kg/m^3)
1	1.4	115	282	1700
2	2.8	220	539	1700
3	∞	315	772	1700

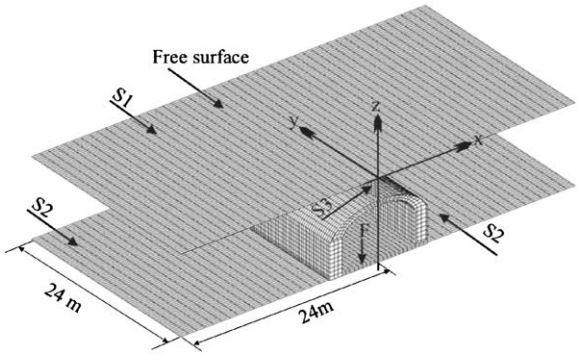

Fig. 4. The tunnel, the non-moving force, and the free surface.

x- and z-directions. Only four rigid-body modes are found instead of six, since the rigid-body rotations around the x- and z-axis do not satisfy the periodicity conditions. Modes 11 and 17 are shown in Figs. 5 and 6, respectively.

A convergence analysis is carried out to determine the number of modes needed for an accurate representation of the harmonic response of the tunnel–soil system. The vertical displacement at the point (0,0,0) on the free surface is considered. Fig. 7 shows the value of the integral of the norm of this displacement over the frequency interval between 0.1 and 80.1 Hz. It follows from this figure that convergence is assured if 30 modes of the tunnel are accounted for. The eigenfrequency of the 30th mode is equal to 224.8 Hz.

3.3. The periodic boundary element method

The soil impedance is computed using the periodic boundary element method. The Green–Floquet fundamental solution is computed using a summation on $2N_c + 1$ terms in Eq. (39). Fig. 8 shows the real part of element (11,11) of the soil impedance matrix in the frequency range from 0.1 to 80.1 Hz, for $\kappa = 0$ and for $N_c = 43$, 101 and 160, respectively. The case of $N_c = 101$, corresponding to 203 terms in the summation of Eq. (39), will be used in the following.

According to Eq. (16), a computation in the range of wavenumbers from $-\pi/L$ to π/L is necessary. For the low frequencies (up to 15 Hz), however, it has been observed that a

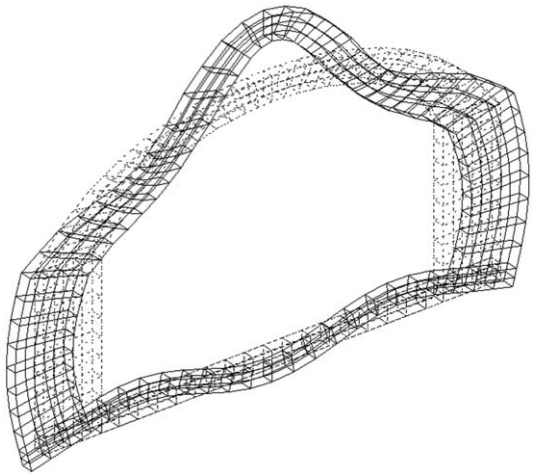

Fig. 5. Mode 11 of the reference cell of the tunnel at 57.6 Hz (displacements in the x- and z-directions only).

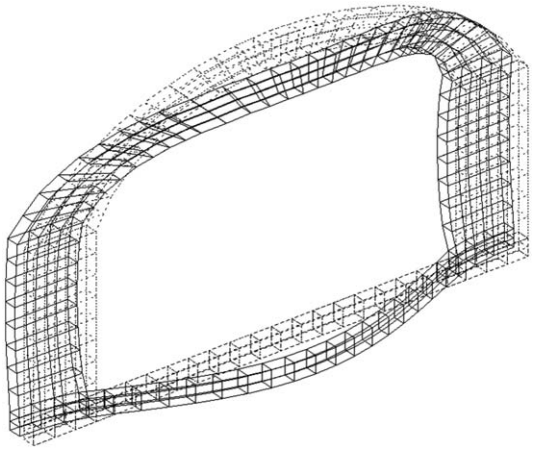

Fig. 6. Mode 17 of the reference cell of the tunnel at 101.5 Hz (displacements in the y-direction only).

computation in the wavenumber range from $-0.6\,\mathrm{m}^{-1}$ to $0.6\,\mathrm{m}^{-1}$ is sufficient, since the solution is rapidly decreasing for increasing κ, as shown in Fig. 9. A sampling interval in the wavenumber domain $\Delta\kappa = 0.015\,\mathrm{m}^{-1}$ is used. For the higher frequencies (from 15 up to 80 Hz), it is more suitable to perform computations in the range of slownesses $p = \kappa/\omega$ from -0.004 to $0.004\,\mathrm{s/m}$, as shown in Fig. 10, where slowness is defined as the inverse of the phase speed in the longitudinal direction. A sampling interval $\Delta p = 10^{-4}\,\mathrm{s/m}$ in the slowness domain is used.

Based on the symmetry of the generic cell, a solution strategy has been developed to avoid the computation of the solution for negative wavenumbers or slownesses. The system of equations (24) is only solved for the positive wavenumbers or slownesses. The inverse Floquet transformation (16) is computed afterwards accounting for the symmetry. A trapezoidal integration scheme is used.

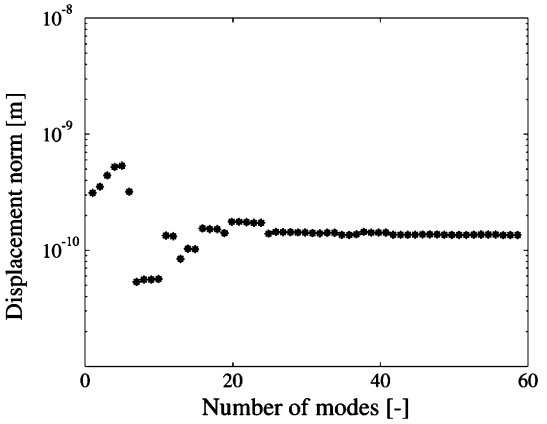

Fig. 7. Integral of the norm of the vertical displacement at the point (0,0,0) on the free surface over the frequency interval between 0.1 and 80.1 Hz as a function of the number of tunnel modes.

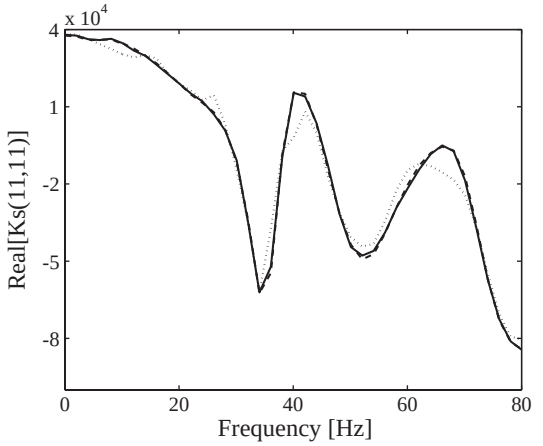

Fig. 8. Real part of the element (11,11) of the soil impedance matrix for $p = 0$ s/m as a function of the excitation frequency computed with $N_c = 43$ (dotted line), $N_c = 101$ (solid line) and $N_c = 160$ (dashed line) terms in the summation for the Green–Floquet fundamental solution.

3.4. The generalized impedance of the tunnel and the soil

Fig. 11 shows the real part of the element (11,11) of the tunnel impedance matrix $\mathbf{K}_t(\kappa) - \omega^2\mathbf{M}_t(\kappa)$ in the slowness range from 0 to 0.007 s/m and the frequency range from 0.1 to 80.1 Hz. The impedance approximately increases with the square of the wavenumber $\kappa = p\omega$. For small values of the slowness p, the inertial term is dominant: the real part of the impedance becomes negative and decreases with the frequency as ω^2 (Fig. 12).

Figs. 13 and 14 show the real and the imaginary part of the element (11,11) of the generalized soil impedance matrix in the slowness range from 0 to 0.007 s/m and for frequencies between 0.1 and 80.1 Hz. The shape of the soil impedance is less regular than the shape of the generalized tunnel impedance. As for the tunnel, the soil is stiffer as κ increases. The inertial effect can also be

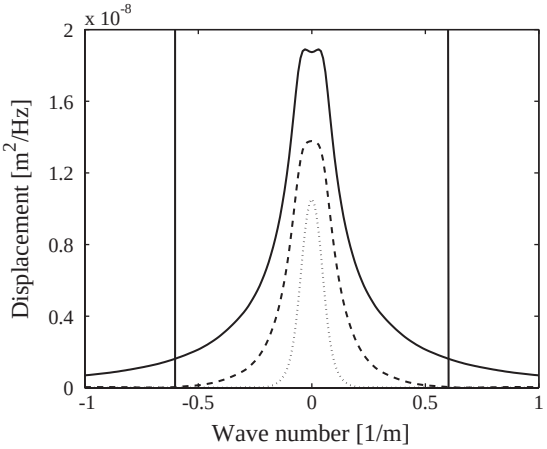

Fig. 9. Amplitude of the vertical displacement at the point $(-0.50, -0.15, -8.25)$ on the tunnel invert directly under the force (solid line), the point $(-2.50, -0.15, -8.25)$ on the tunnel invert at 2 m from the force (dashed line) and the point $(0, -0.15, -2.30)$ on the tunnel roof (dotted line) as a function of the wavenumber for a harmonic excitation at 5 Hz.

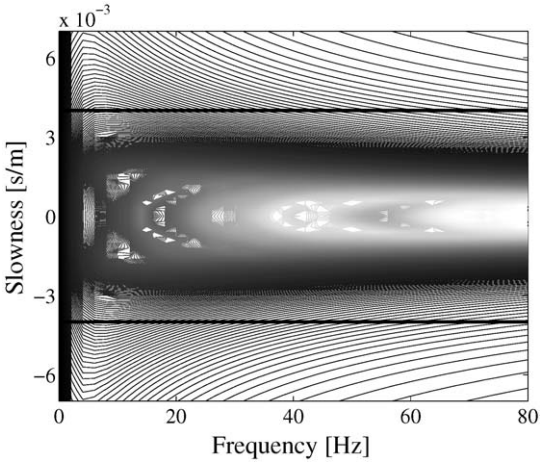

Fig. 10. Amplitude of the vertical displacement at the point $(-0.50, -0.15, -8.25)$ on the tunnel invert directly under the force as a function of the slowness and the excitation frequency.

observed for low values of the slowness. The damping almost disappears for large values of the slowness.

4. Harmonic response of the tunnel–soil system

Harmonic loads at different frequencies are applied on the invert of the tunnel. Fig. 15 shows the transfer functions for the displacements at the points $(0, 0, 0)$, $(-2, 0, 0)$, $(-10, 0, 0)$ and $(-20, 0, 0)$ along the free surface in the same cross-section where the load is applied, while Fig. 16

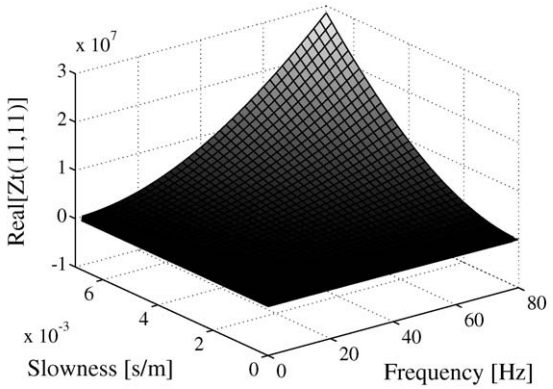

Fig. 11. Real part of the element (11,11) of the generalized tunnel impedance matrix $\mathbf{K}_t(\kappa) - \omega^2\mathbf{M}_t(\kappa)$ as a function of the slowness and the excitation frequency.

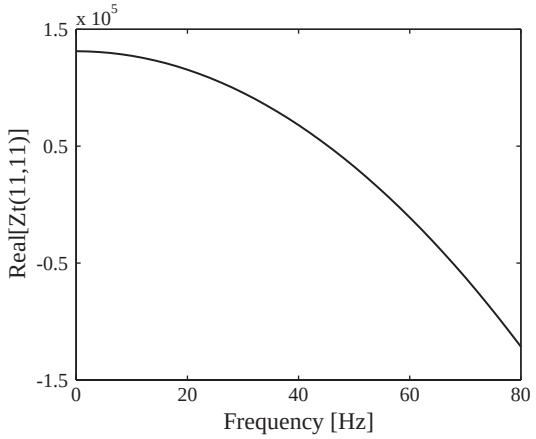

Fig. 12. Real part of the element (11,11) of the generalized tunnel impedance matrix $\mathbf{K}_t(\kappa) - \omega^2\mathbf{M}_t(\kappa)$ for a slowness $p = 0\,\mathrm{s/m}$ as a function of the excitation frequency.

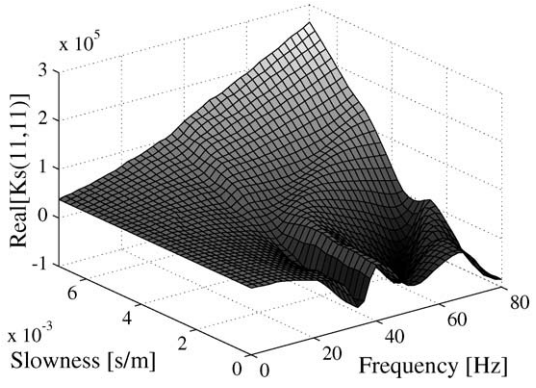

Fig. 13. Real part of the element (11,11) of the soil impedance matrix as a function of the slowness and the excitation frequency.

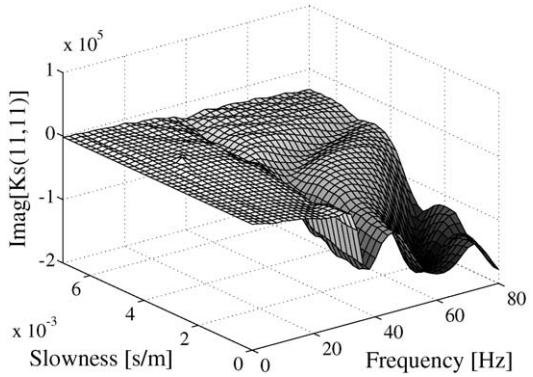

Fig. 14. Imaginary part of the element (11,11) of the soil impedance matrix as a function of the slowness and the excitation frequency.

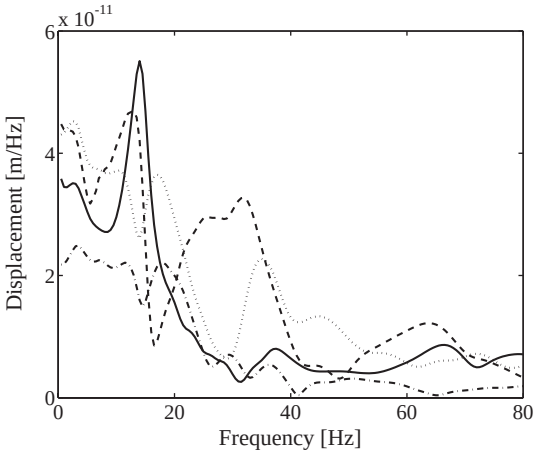

Fig. 15. Amplitude of the vertical displacement at the points along the free surface with coordinates $(0,0,0)$ (solid line), $(-2,0,0)$ (dashed line), $(-10,0,0)$ (dotted line) and $(-20,0,0)$ (dashed–dotted line) as a function of the excitation frequency.

shows the transfer functions for the displacements at the point $(-2.50, -0.15, -8.25)$ on the tunnel invert, at the point $(0, -0.15, -2.30)$ at the tunnel apex and at the point $(0,0,0)$ on the free surface. Figs. 15 and 16 show an important peak at 14 Hz. This maximum appears for points on the free surface close to the tunnel and on the tunnel roof.

The displacements are also computed in all points of the mesh of Fig. 4 in order to visualize the harmonic response of the tunnel and the soil. In this figure, the generic cell is repeated 80 times in the positive y-direction. For post-processing purposes, three additional surfaces in the soil have been meshed: the free surface S1, the horizontal surfaces S2 at the depth of the tunnel, and a vertical surface S3 between the free surface and the middle of the tunnel top. First, the displacements of all points in the generic cell are computed in the wavenumber-frequency domain using the elastodynamic representation theorem. Second, when all displacements in the generic

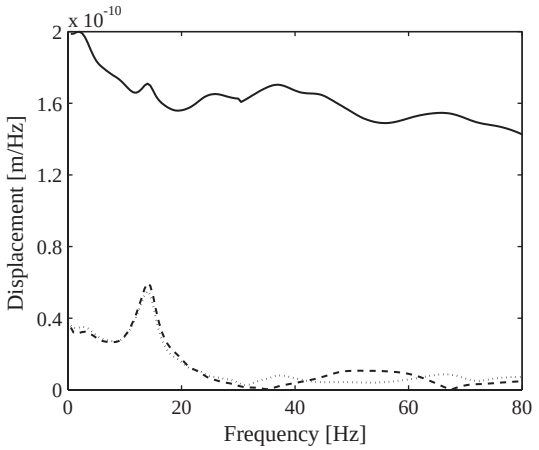

Fig. 16. Amplitude of the vertical displacement at the point $(-2.50, -0.15, -8.25)$ on the tunnel invert directly under the force (solid line), the point $(0, -0.15, -2.30)$ at the tunnel apex (dashed line) and the point $(0, 0, 0)$ on the free surface above the tunnel apex (dotted line) as a function of the excitation frequency.

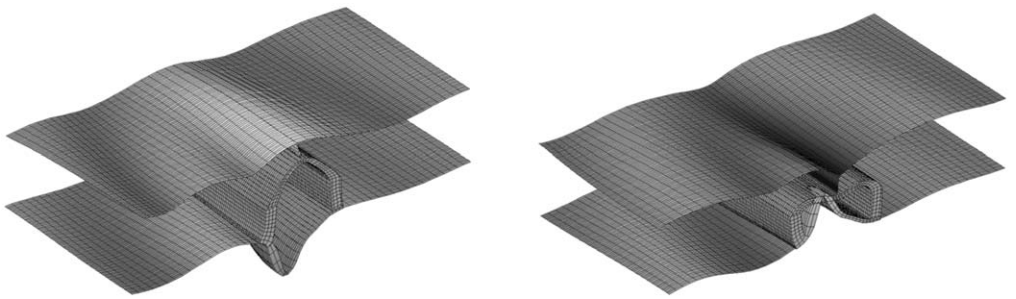

Fig. 17. Real part of the displacements of the tunnel and the soil due to a harmonic excitation on the tunnel invert at 14 Hz at $t = 0$ (left) and $t = T/2$ (right).

cell are known, the inverse Floquet transform is used to compute the displacements in all points of the mesh over a length of 24 m. When all transfer functions are known in the wavenumber-frequency domain on the generic cell, a computation of the Floquet inverse transform gives the transfer functions for all points of this mesh.

Fig. 17 shows the displacements of the tunnel and the soil in all points of this mesh due to a harmonic excitation on the tunnel invert at 14 Hz at $t = 0$ and $T/2$, with $T = 1/14$ s the period of the excitation. The grey shading on the figure is relative to the vertical displacements and is 10 times exaggerated on the surfaces in the soil if compared to the tunnel displacements. The figure demonstrates that the soil above the tunnel and the tunnel roof move in phase. At this frequency, the soil above the tunnel can be considered as an equivalent mass, while the tunnel is an equivalent spring. The peak at 14 Hz corresponds to the resonance peak of this mass–spring system, while damping is due to the radiation of waves away from the tunnel (Fig. 17).

At higher frequencies, the propagation of waves away from the tunnel dominates, as shown in Fig. 18. Starting from the source point, bending waves are propagating on the tunnel invert along the longitudinal axis of the tunnel, as well as in the perpendicular direction, before they are reflected by the tunnel walls. In the soil, propagation along and perpendicular to the tunnel axis can be observed. On the free surface above the tunnel, higher phase velocities are observed along the tunnel axis than in the direction perpendicular to the tunnel, resulting in an elliptical wavefront (Fig. 18). Waves propagating away from the tunnel at the depth of the tunnel invert can also be observed on the surface S2.

Fig. 19 shows the variation of the phase of the vertical displacements at the free surface along the line $x = -4$ m parallel to the y-axis at an excitation frequency of 80 Hz. A wavelength of 24 m can be estimated along the y-axis, corresponding to a phase velocity of 1920 m/s. Similarly, the phase velocity along the x-axis perpendicular to the tunnel can be estimated as 650 m/s. The high phase velocities along the y-axis correspond to leaky waves of the system consisting of the roof

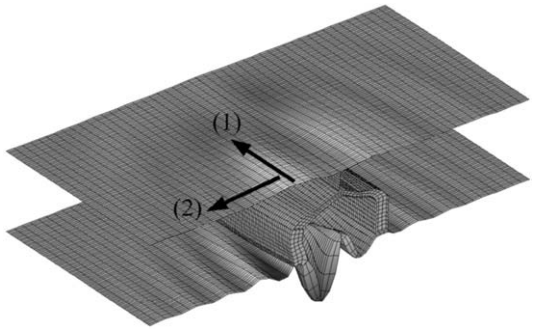

Fig. 18. The displacements of the tunnel and the soil due to a harmonic excitation on the tunnel invert at 80 Hz: (1) fast wave propagation along the tunnel axis and (2) slower wave propagation in the direction perpendicular to the tunnel axis.

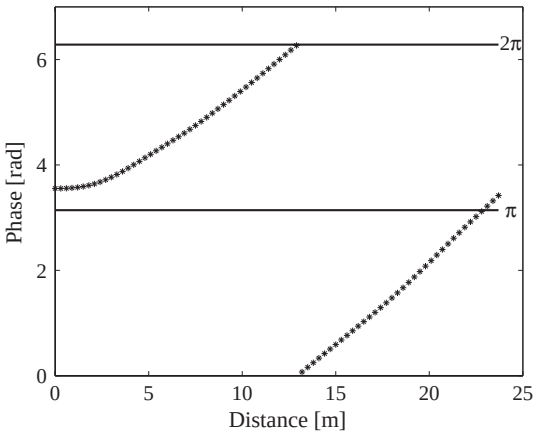

Fig. 19. The phase of the vertical displacements at the free surface along the line $x = -4$ m as a function of the distance y along the tunnel due to a harmonic excitation on the tunnel invert at 80 Hz.

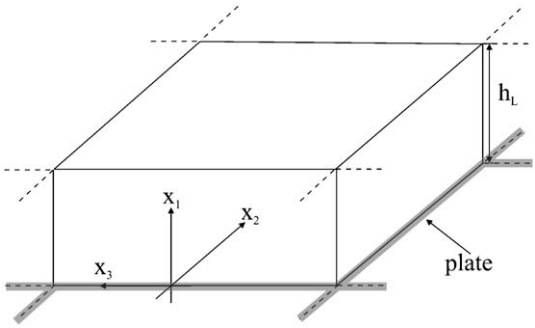

Fig. 20. Simplified model of an infinite layer on an infinite plate.

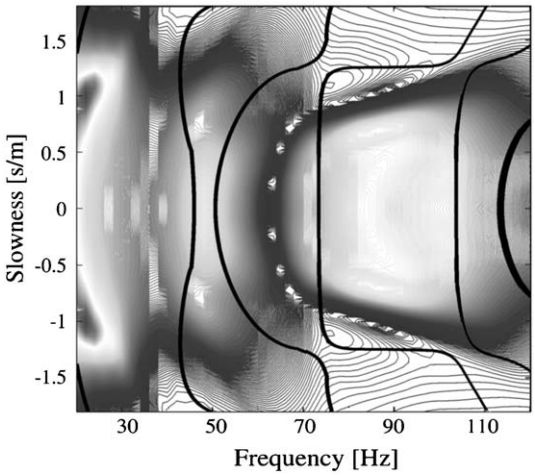

Fig. 21. Response of the tunnel as a function of the slowness and the excitation frequency. Superimposed on the same graph are the dispersion curves of the simplified model.

vault and the top soil layer. This can be demonstrated by comparing the dispersion curves of an infinite soil layer on an infinite plate, as shown in Fig. 20, and the displacement response of the tunnel. The dispersion curves are computed for a soil layer with the average characteristics of the two soil layers above the tunnel, on top of a plate with the characteristics of the tunnel roof. The dispersion curves are plotted in Fig. 21 on top of the tunnel response. The maxima of the response are found in the vicinity of the dispersion curves.

5. Transient response of the tunnel–soil system

This section is devoted to the transient response of the tunnel–soil system due to a hammer impact on the tunnel invert. The impact force is modelled in the time domain by means of a very narrow Gaussian function. The Fourier transform of a Gaussian function is a Gaussian function,

however, with a non-vanishing quasi-static component. Due to the limitations related to the computation of the Green functions of a layered half-space, the 3D tunnel–soil interaction model cannot compute the quasi-static response. In order to overcome this problem, two hammer impacts are applied, the first in the downward z-direction and the second in the upward z-direction, so that the quasi-static component vanishes. The applied force has the following form in the time domain:

$$f(t) = -\exp\left(-\frac{(t-t_1)^2}{T^2}\right) + \exp\left(-\frac{(t-t_2)^2}{T^2}\right). \tag{40}$$

Fig. 22 shows the time history of this force with parameters $t_1 = 0.1\,\text{s}$, $t_2 = 1.1\,\text{s}$ and $T = 0.0025\,\text{s}$. The Fast Fourier Transform algorithm is used to perform the transformation between the time and the frequency domain. As this technique requires a finer sampling in the frequency domain, a period of 2 s is chosen, corresponding to a narrow bandwidth of 0.5 Hz. The time step is equal to 0.0025 s, corresponding to a Nyquist frequency of 200 Hz. Fig. 23 shows the frequency content of the impact force. The oscillating behavior is due to the application of two pulses.

Figs. 24 and 25 show two snapshots of the displacements due to the first (downward) hammer impact at times $t = 0.1\,\text{s}$ (moment of impact) and $t = 0.16\,\text{s}$, respectively. Fig. 25 shows that, after the impact, a strong and fast front of vertical downward displacements propagates away from the tunnel, immediately followed by a front of vertical upward displacements.

Fig. 26 shows a seismogram of the vertical displacements at the free surface on the line $y = 0$ with negative x-coordinates. Five different types of waves can be identified. All waves are emitted by the tunnel and are propagating in the layered half-space.

The wave field can be compared to waves that are induced by single forces at different depths of the layered half-space. The same Gaussian impact forces are therefore also applied at depths $z = 0$, -3 and $-9\,\text{m}$ in a layered half-space, corresponding, respectively, to the free surface, the depth of the tunnel roof, and the depth of the tunnel invert. The transfer functions in the slowness-frequency domain are presented in Figs. 27, 29 and 31, while the seismograms with the vertical displacements at the free surface are given in Figs. 28, 30 and 32.

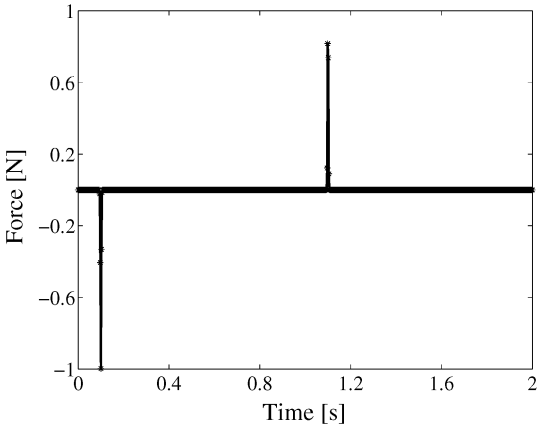

Fig. 22. Time history of the Gaussian impact force applied to the tunnel invert ($t_1 = 0.1\,\text{s}$, $t_2 = 1.1\,\text{s}$ and $T = 0.0025\,\text{s}$).

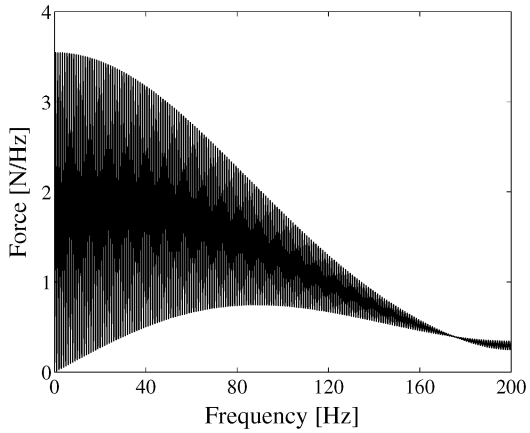

Fig. 23. Frequency content of the Gaussian impact force applied to the tunnel invert.

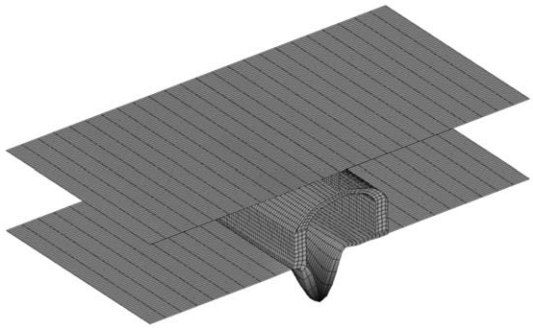

Fig. 24. Displacements of the tunnel and the soil at $t = 0.1$ s (moment of impact) due to a Gaussian impact force on the tunnel invert.

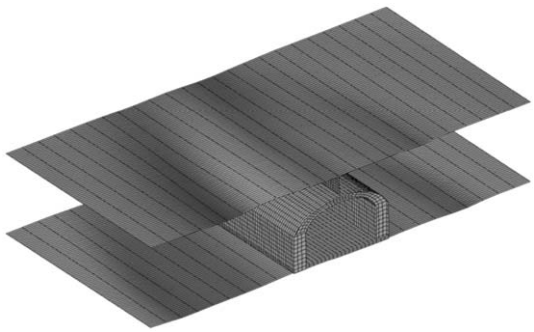

Fig. 25. Displacements of the tunnel and the soil at $t = 0.16$ s (0.06 s after impact) due to a Gaussian impact force on the tunnel invert.

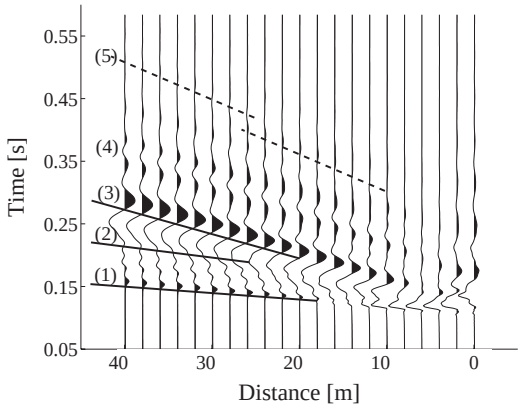

Fig. 26. Seismogram of the vertical displacements at the free surface on the line $y = 0$ with negative x coordinates due to a Gaussian impact force on the tunnel invert.

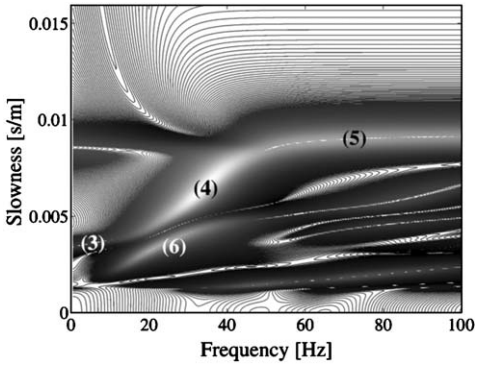

Fig. 27. Transfer function in the ω–p domain for a Dirac impulse at a depth of 0 m.

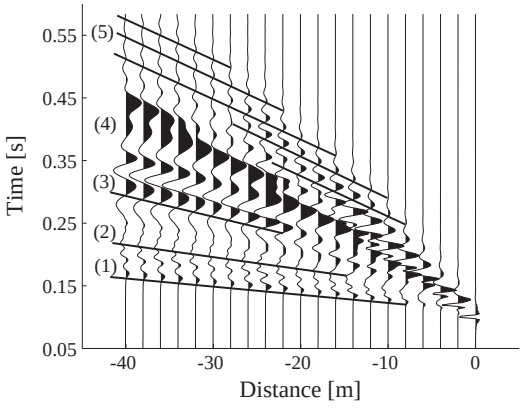

Fig. 28. Seismogram of the vertical displacements at the free surface for a Gaussian impact force at a depth of 0 m.

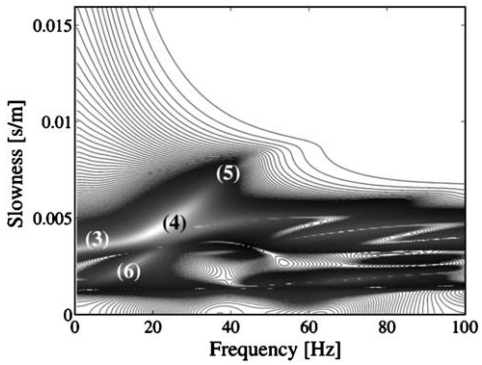

Fig. 29. Transfer function in the ω–p domain for a Dirac impulse at a depth of 3 m.

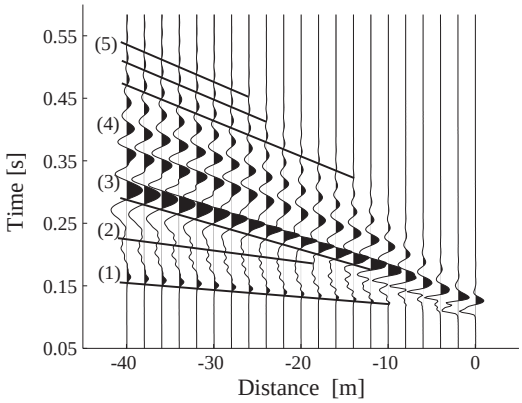

Fig. 30. Seismogram of the vertical displacements at the free surface for a Gaussian impact force at a depth of 3 m.

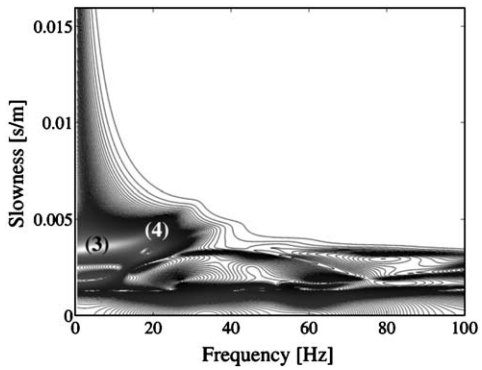

Fig. 31. Transfer function in the ω–p domain for a Dirac impulse at a depth of 9 m.

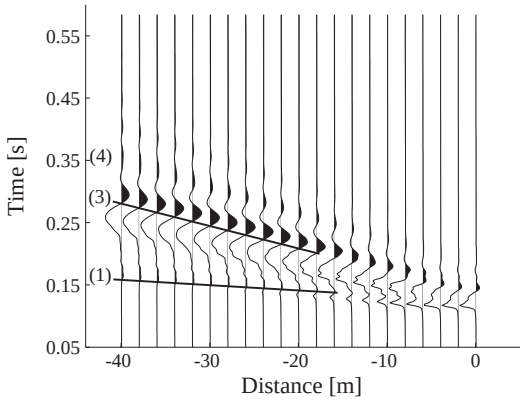

Fig. 32. Seismogram of the vertical displacements at the free surface for a Gaussian impact force at a depth of 9 m.

As observed on these figures, only forces at the free surface are generating Rayleigh waves of the first slow layer at high frequencies (event (5) in Figs. 27 and 28), whereas for an excitation at depth, the Rayleigh waves of the underlying half-space at low frequencies are excited (event (3) in the ω–p domain and in the seismograms). Two important peaks (4) and (6) in the ω–p domain cause highly dispersive waves (4) in the seismograms, related to the Rayleigh wave of the stratigraphy between the Rayleigh wave of the first layer and the Rayleigh wave of the half-space. Waves (1) and (2) are classical refracted waves on top of the underlying stratified half-space.

It can now be understood that the tunnel's bottom plate excites the Rayleigh resonance of the half-space at low frequencies (event (3) in Fig. 26) and generates body waves in the fast half-space (event (1) in Fig. 26). The upper parts of the tunnel walls and the tunnel roof generate refracted waves in the layered half-space (event (2) in Fig. 26). The upper part of the tunnel still contributes to Rayleigh waves of the half-space at low frequencies, but also to the dispersive Rayleigh waves (4) at medium frequencies and to the high-frequency Rayleigh waves (5) of the first layer.

6. Conclusion and discussion on future work

To the authors' knowledge, this paper is the first attempt to model, both in the frequency and the time domain, the wave field radiated in a horizontally layered soil by a point force applied on the invert of a shallow cut-and-cover tunnel, fully accounting for the three-dimensional geometry of the tunnel, as required in the frequency band between 1 and 100 Hz. The periodic approach, originally proposed for applications in earthquake engineering in the frequency range between 0 and 10 Hz, allows to model wave propagation over tens of wavelengths both in the longitudinal and the transverse directions of the tunnel, which would have been impossible with standard three-dimensional finite element and boundary element formulations.

The convergence of the numerical results has been assessed. It has been shown that the response of the tunnel and the soil, in the immediate vicinity of the tunnel, is strongly affected by the presence of the free surface and the layering. In particular, a low-frequency resonance of the soil mass above the tunnel has been identified. Moreover, the results have revealed a high anisotropy

of the propagation of waves in the directions along and perpendicular to the tunnel. High-phase velocities in the longitudinal direction have been attributed with a reasonable agreement to guided waves inside the system of the tunnel roof and the top layers. It has also been shown that the radiated wavefield at some distance from the tunnel is mainly governed by refracted waves and generalized Rayleigh waves in the layered medium. The high-frequency filtering induced by the embedment of the source is governed by the depth of the tunnel roof rather than the depth of the tunnel invert. As a conclusion, the wavefield induced by a point force applied at the bottom of the tunnel cannot be approximated by an equivalent force in the soil at the corresponding depth, as an additional force at the depth of the tunnel roof is needed to mimic the coupled numerical solution.

As mentioned already in the introduction, the 3D Green functions of the coupled tunnel–soil system are the basic ingredient for a more complex model that incorporates moving sources, accounting for vehicle–track interaction and transmission to nearby buildings. These transfer functions can also be compared with experimental results since they are not affected by the randomness of rail–wheel contact or the uncertainties on the dynamic response of passing trains. Such a comparison will soon be carried out in the CONVURT project. However, such a validation still highly depends on the uncertainties on the soil and tunnel properties. It is believed that model updating using the first identified resonance of the tunnel roof will allow for a good calibration of the tunnel stiffness, whereas SASW and down-hole tests are providing reliable estimations of the dynamic soil properties. A systematic analysis of the propagation of uncertainties has to be carried out, as proposed by Clouteau et al. [24] and Lombaert et al. [25]. In particular, the efficiency of the proposed periodic approach will allow for Monte Carlo simulations with random properties of the soil and the tunnel, including random fluctuations with a correlation length that is smaller than the length of the periodic cell.

Acknowledgements

The results presented in this paper have been obtained within the frame of the European Project G3RD-CT-2000-00381 CONVURT "The Control of Vibration from Underground Railway Traffic" in the Fifth Framework Research Programme Growth. The project has 11 partners from metro railways, industry, consultancy and universities and receives grant funding from the European Community. More information on the project can be found on the web site of the project at http://www.convurt.com.

References

[1] D. Aubry, D. Clouteau, G. Bonnet, Modelling of wave propagation due to fixed or mobile dynamic sources, in: N. Chouw, G. Schmid (Eds.), *Workshop Wave '94, Wave Propagation and Reduction of Vibrations*, Rühr University, Bochum, Germany, December 1994, pp. 109–121.

[2] X. Sheng, C.J.C. Jones, M. Petyt, Ground vibration generated by a load moving along a railway track, *Journal of Sound and Vibration* 228 (1) (1999) 129–156.

[3] A.M. Kaynia, C. Madshus, P. Zackrisson, Ground vibration from high speed trains: prediction and countermeasure, *Journal of Geotechnical and Geoenvironmental Engineering* 126 (6) (2000) 531–537.

[4] V.V. Krylov, Effects of track properties on ground vibrations generated by high-speed trains, *Acustica-Acta Acustica* 84 (1) (1998) 78–90.
[5] G. Lombaert, G. Degrande, D. Clouteau, Numerical modelling of free field traffic induced vibrations, *Soil Dynamics and Earthquake Engineering* 19 (7) (2000) 473–488.
[6] G. Lombaert, G. Degrande, D. Clouteau, The influence of the soil stratification on free field traffic induced vibrations, *Archive of Applied Mechanics* 71 (10) (2001) 661–678.
[7] G. Degrande, G. Lombaert, An efficient formulation of Krylov's prediction model for train induced vibrations based on the dynamic reciprocity theorem, *Journal of the Acoustical Society of America* 110 (3) (2001) 1379–1390.
[8] K. Knothe, Y. Wu, Receptance behaviour of railway track and subgrade, *Archive of Applied Mechanics* 68 (1998) 457–470.
[9] P. Van den Broeck, G. Degrande, G. De Roeck, A prediction model for the ground-borne vibrations due to railway traffic, in: H. Grundmann (Ed.), *Proceedings of the 5th European Conference on Structural Dynamics*, Munich, Germany, September 2002, pp. 503–508.
[10] A. Kraft, Prediction of vibrations of underground railway, Report to ISO TC 108/SC 2/WG 3, TÜV Rheinland, 1996.
[11] B. Hemsworth, Reducing groundborne vibrations: state of the art study, *Journal of Sound and Vibration* 231 (3) (2000) 703–709.
[12] K.H. Chua, K.W. Lo, T. Balendra, Building response due to subway train traffic, *Journal of Geotechnical Engineering* 121 (11) (1995) 747–754.
[13] A.V. Metrikine, T. Vrouwenvelder, Surface ground vibration due to a moving train in a tunnel: two-dimensional model, *Journal of Sound and Vibration* 234 (1) (2000) 43–66.
[14] H.E.M. Hunt, Modelling of rail vehicles and track for calculation of ground vibration transmission into buildings, *Journal of Sound and Vibration* 193 (1) (1996) 185–194.
[15] A.A. Stamos, D.E. Beskos, Dynamic analysis of large 3-D underground structures by the BEM, *Earthquake Engineering and Structural Dynamics* (1995) 1–18.
[16] A.A. Stamos, D.E. Beskos, 3-D seismic response analysis of long lined tunnels in half-space, *Soil Dynamics and Earthquake Engineering* 15 (1996) 111–118.
[17] D. Clouteau, G. Degrande, G. Lombaert, Some theoretical and numerical tools to model traffic induced vibrations, in: N. Chouw, G. Schmid (Eds.), *Proceedings of the International Workshop Wave 2000*, *Wave Propagation, Moving Load, Vibration Reduction*, Ruhr University, Germany, December 2000, A.A. Balkema, Rotterdam, 2000, pp. 13–27.
[18] D. Clouteau, G. Degrande, G. Lombaert, Numerical modelling of traffic induced vibrations, *Meccanica* 36 (4) (2001) 401–420.
[19] D. Clouteau, M.L. Elhabre, D. Aubry, Periodic BEM and FEM-BEM coupling: application to seismic behaviour of very long structures, *Computational Mechanics* 25 (2000) 567–577.
[20] D. Clouteau, D. Aubry, *Computational Soil–Structure Interaction*, Kluwer, Dordrecht, 2003, pp. 61–125.
[21] D. Clouteau, D. Aubry, M.L. Elhabre, E. Savin, Periodic and stochastic BEM for large structures embedded in an elastic half-space, in: M. Bonnet, A.-M. Sandig, W.L. Wendland (Eds.), *Mathematical Aspects of Boundary Element Methods*, Research Notes in Mathematics Series, vol. 414, CRC Press, London, 1999, pp. 91–102.
[22] M.L. Elhabre, Modélisation de l'Interaction Sismique Sol-fluide-parois Moulées Suivant une Approche Périodique, PhD Thesis, Laboratoire de Mécanique des Sols, Structures et Matériaux, Ecole Centrale de Paris, 2000.
[23] L. Pyl, G. Degrande, Determination of the dynamic soil characteristics with the SASW method at the site of Cité universitaire in Paris, Report BWM-2002-08, Department of Civil Engineering, Katholieke Universiteit Leuven, October 2002, CONVURT EC-Growth Project G3RD-CT-2000-00381.
[24] D. Clouteau, T.M. Al-Hussaini, G. Degrande, H. Hunt, Stochastic modelling of traffic induced vibrations, in: *First Albert Caquot International Conference. Modelling and Simulation in Civil Engineering*: *from Practice to Theory*, Paris, France, October 3–5, 2001.
[25] G. Lombaert, G. Degrande, D. Clouteau, The non-stationary freefield response for a moving load with a random amplitude, *Journal of Sound and Vibration* 278 (3) (2004) 611–635.